Journal of
Marine Science and Engineering

MDPI

Article

Numerical Investigation on the Ventilated Supercavity around a Body under Free Surface Effect

Yuchang Zhi [1], Jiemin Zhan [1], Renfang Huang [2,*], Yiwei Wang [2,3,4] and Ning Li [5,6]

[1] Department of Applied Mechanics and Engineering, Shenzhen Campus of Sun Yat-sen University, No. 66, Gongchang Road, Guangming District, Shenzhen 518107, China
[2] Key Laboratory for Mechanics in Fluid Solid Coupling Systems, Institute of Mechanics, Chinese Academy of Sciences, Beijing 100190, China
[3] School of Future Technology, University of Chinese Academy of Sciences, Beijing 100049, China
[4] School of Engineering Science, University of Chinese Academy of Sciences, Beijing 100049, China
[5] Marine Design and Research Institute of China, Shanghai 200011, China
[6] Science and Technology on Waterjet Propulsion Laboratory, Shanghai 200011, China
* Correspondence: hrenfang@imech.ac.cn

Abstract: Reducing vessel resistance by using ventilated cavities has been a highly researched topic in the marine industry. There is limited literature on ventilated supercavities near the free surface, which indicates that their dynamic behavior is more complex than conventional ventilated cavities due to the effect of the free surface. This paper employs numerical simulations to study the dynamic behavior of the ventilated supercavity, taking into account the effect of the free surface. Numerical simulations can predict gas leakage behaviors, cavity geometry, and internal flow structures. The influence of the free surface shortens the length of the ventilated cavity and increases the diameter. The presence of the free surface mainly changes the vertical velocity distribution between the free surface and the cavity. The results show that there are two typical gas leakage mechanisms under different immersion depths: twin-vortex tube leakage mode and re-entrant jet leakage mode. The internal flow field of ventilated supercavity is classified into three regions: the internal boundary layer, the ventilation influence region, and the reverse flow region. As the distance between the free surface and the ventilated supercavity decreases, the ventilated supercavity is affected by both the free surface effect and the gravity effect.

Keywords: ventilated supercavity; free surface; dynamic behavior; gas leakage

check for updates

Citation: Zhi, Y.; Zhan, J.; Huang, R.; Wang, Y.; Li, N. Numerical Investigation on the Ventilated Supercavity around a Body under Free Surface Effect. *J. Mar. Sci. Eng.* **2023**, *11*, 912. https://doi.org/10.3390/jmse11050912

Academic Editor: Alon Gany

Received: 28 March 2023
Revised: 21 April 2023
Accepted: 22 April 2023
Published: 24 April 2023

1. Introduction

Reducing vessel resistance by using ventilated cavities has been a highly researched topic in the marine industry [1–4]. Numerous studies on ventilated cavities have demonstrated that injecting non-condensable gas around the submarine surface can create a cavity at low speeds and high environmental pressures, thereby effectively reducing the frictional resistance of the submarine [5–8]. This is achieved by creating air-frictional resistance rather than water-frictional resistance. This technology has been successfully applied to large vessels [9]. Therefore, studying the ventilated cavitating flow is crucial for designing and optimizing the next generation of submarines.

Experimental measurements are one of the most effective methods for investigating the physical mechanisms of ventilated cavity flow [10,11]. High-speed imaging systems and flow measurement devices can be used during these experiments to obtain information on the gas leakage behavior, the cavity geometry, and the flow structures around the device. Additionally, pressure sensors and force sensors can be used to measure the pressure inside the ventilated cavity and the resistance of the marine structure, respectively [12]. Karn et al. [13,14] conducted ventilated cavity flow experiments and obtained information on the gas leakage behavior and the cavity geometry, as well as the cavity flow transition patterns, using a high-speed camera and a PIV flow field measurement device [15]. The results indicated that analyzing the internal flow structure inside the cavity is helpful for further understanding the flow regime and its transition patterns [16]. Qin et al. [17] experimentally studied the partial ventilation of a submarine flat plate. They captured the shape of the ventilated cavity under different working conditions using an imaging system and used multiple parameters to form a ventilated cavity phase diagram, which provided insights into the physical mechanisms of the cavity state transition. Barbara et al. [18] developed a high-quality imaging and force measurement system that consisted of a measurement balance, a pressure sensor, and a high-speed camera. Using this system, they conducted an experimental study on the ventilated cavity flow over a 3D wall-mounted fence and obtained the flow pattern and pressure distribution inside the cavity. Experimental results showed that the ventilation rate and cavitation number significantly affected the cavity topology and resistance of the 3D wall-mounted fence. While techniques such as PIV and high-speed photography can be used to obtain some flow parameters of the cavity, measuring the internal flow field of the cavity influenced by the free surface is still challenging.

Understanding the dynamic behavior of the ventilated cavity around a submarine body requires knowledge of its internal flow and 3D geometry under different flow conditions [19]. However, experimental measurement of this information is challenging. Instead, numerical simulations offer a more effective way to obtain accurate gas leakage behavior, geometry, and internal flow structure of the cavity, enabling a deeper understanding and analysis of its behavior [20–22]. The numerical simulation can also provide a good analysis of the transient fluid dynamics of the cavity, including pressure, velocity, wake, and vorticity field [23,24].

In a study by Lv et al. [25], numerical simulations were conducted on the ventilated cavity surrounding an axisymmetric cylinder. The results showed that the simulated cavity geometry agreed with the experimental findings. The ventilated cavity was found to consist of three distinct parts: the internal boundary layer near the gas-water interface, the ventilation influence region affected by injected air, and the reverse flow region opposite to the flow direction. Ji et al. [26] proposed a three-component cavitation model that is well suited for simulating ventilated cavity flow. The method is capable of accurately simulating the internal flow characteristics and the geometric shape of the cavity, producing results that are consistent with experimental results. Jiang et al. [27] simulated the geometric shape of a ventilated cavity and the submarine drag characteristics, achieving agreement with experimental findings. Furthermore, they proposed a resistance reduction scheme based on the simulation results. Zhang et al. [28] analyzed the mechanism of ventilated cavity transformation and the associated pressure evolution, and found that non-constant evolution of the shedding of the vortex structures is the main cause of induced pressure waves. Wang et al. [29] conducted both experimental and numerical studies of partially ventilated cavities and supercavities, providing insight into the physical mechanisms behind cavity transformation by analyzing the cavity geometry and the internal flow field structure.

Previous literature on vaporous cavities or ventilated cavities near the free surface indicates that the dynamic behavior of these cavities is affected by the presence of the free surface [30–33]. Liu et al. [34] studied the ventilated supercavity generated by a cavitator after horizontal movement close to the free surface. The results showed that the gas leakage mode and the cavity surface curvature were affected by the presence of the free surface, and the length-to-width ratio of the cavity also decreased with increasing immersion depth. Moltani et al. [35] conducted experimental and numerical investigations into the cavity shape, the gas leakage behavior, and the model drag coefficient under the influence of the free surface. As the Froude number increased, the dimensions of the ventilated cavity, including its length and diameter, increased, while the drag coefficient decreased. Furthermore, the model drag coefficient increased with higher immersion depths. Xu et al. [36] compared the cavitation flow regime with the influence of the free surface. The cavity shape is asymmetric and has three-dimensional flow features compared to the case of infinite water depth. Xu et al. [37–39] studied the cavitation characteristics surrounding an obtuse body near the free surface. The calculated cavity geometry and shedding process were consistent with the experiment. A decrease in immersion results in a significant change in the cavity geometry due to the presence of the free surface. Zhi et al. [40] conducted a study on a vaporous cavity around a surface-piercing hydrofoil. They found that the vaporous cavity under the effect of free surface exhibits three-dimensional characteristics and its evolution is closely related to the re-entrant jet. It was found in the available literature that the numerical simulation technique is feasible for studying the interaction between the free surface and the ventilated cavity.

Currently, the research on the interaction between the ventilated supercavity and the free surface is limited, with most studies focusing on the changes in the supercavity geometry and model resistance. The mechanism underlying the interaction between the ventilated supercavity and free surface is not yet fully understood. Therefore, it is essential to investigate the gas leakage behavior, geometry, and internal flow structure of the cavity near the free surface. This paper first discusses the ventilated supercavity geometry under the influence of the free surface. Next, it examines the flow details inside the cavity, the gas leakage behaviors, and the free surface elevation. Finally, it investigates the effect of the ventilated cavity on the free surface and analyzes the underlying mechanism of the interaction between the two. Compared with previous work, the unique contributions in the present paper are: (1) the gas leakage mode and geometric shape evolution of the ventilated cavity under the influence of the free surface are described in detail, and (2) the mechanism of free surface-ventilated cavity interaction is extended.

2. Numerical Approach

2.1. Governing Equations

The numerical simulations were carried out using the commercial CFD code STAR-CCM+ 13.06, which is based on the finite volume method. To obtain the free surface and the ventilated cavity, the continuity equation and the momentum equation were employed [41]:

$$\frac{\partial \rho}{\partial t} + \frac{\partial(\rho u_i)}{\partial x_i} = 0 \tag{1}$$

$$\frac{\partial(\rho u_i)}{\partial t} + \frac{\partial(\rho u_i u_j)}{\partial x_j} = -\frac{\partial p}{\partial x_i} + \frac{\partial}{\partial x_j}\left(\mu\frac{\partial u_i}{\partial x_j} - \rho\overline{u'u'_j}\right) + S_j \tag{2}$$

where u_i denotes velocity component in the i direction, ρ denotes the mixture density of water and air, μ denotes flow viscosity, and p denotes pressure.

$$\rho = \alpha_{\mathrm{a}}\rho_{\mathrm{a}} + (1-\alpha_{\mathrm{a}})\rho_{\mathrm{l}} \tag{3}$$

$$\mu = \alpha_{\mathrm{a}}\mu_{\mathrm{a}} + (1-\alpha_{\mathrm{a}})\mu_{\mathrm{l}} \tag{4}$$

where α represents the proportion of water or air to the volume of the mixture and the subscripts l and a indicate the water and air, respectively.

The standard k-ε turbulence model was applied to solve the equation, where the kinetic energy k and turbulent dissipation rate ε were defined as [42]:

$$\frac{\partial}{\partial t}(\rho k) + \nabla\cdot(\rho k\overline{u}) = \nabla\cdot\left[(\mu + \frac{\mu_t}{\sigma_k})\nabla k\right] + P_k - \rho(\varepsilon - \varepsilon_0) + S_k \tag{5}$$

$$\frac{\partial}{\partial t}(\rho\varepsilon) + \nabla\cdot(\rho\varepsilon\overline{u}) = \nabla\cdot\left[(\mu + \frac{\mu_t}{\sigma_\varepsilon})\nabla\varepsilon\right] + \frac{1}{T_e}C_{\varepsilon 1}P_\varepsilon - C_{\varepsilon 2}f_2\rho(\frac{\varepsilon}{T_e} - \frac{\varepsilon_0}{T_0}) + S_\varepsilon \tag{6}$$

where f_2 represents a damping function, σ_k, σ_ε, $C_{\varepsilon 1}$, and $C_{\varepsilon 2}$ denote model coefficients, $T_e = k/\varepsilon$ represents the large-eddy time scale, and S_k and S_ε are user-specified source terms. Based on the source terms, P_k and P_ε are production terms and T_0 is a specific time-scale:

$$T_0 = \max(\frac{k_0}{\varepsilon_0}, C_{\mathrm{t}}\sqrt{\frac{v}{\varepsilon_0}}) \tag{7}$$

where ν represents the kinematic viscosity, C_{t} represents the model coefficient, and ε_0 represents the ambient turbulence value [43].

2.2. Wave Damping

Due to the w-velocity having a large variation near the free surface and being related to the wave height, to avoid the reflection of free surface waves, one possible approach is to include a term of resistance in the equation for w-velocity [44]:

$$S_z^d = \rho(f_1 + f_2|w|)\frac{e^\kappa - 1}{e^1 - 1}w \tag{8}$$

with:

$$\kappa = \left(\frac{x - x_{sd}}{x_{ed} - x_{sd}}\right)^{n_d} \tag{9}$$

where f_1, f_2, and n_d denote parameters of the damping model, w represents the vertical velocity component, x_{sd} denotes the initiation point for wave damping, and x_{ed} represents the termination point for wave damping [40].

3. Numerical Setup and Description

3.1. Geometric Details and Calculation Process

The model [12] used in the paper consists of a cylinder capped with a hemispherical end and a disk-type cavitator, as shown in Figure 1. This underwater body has a length of 75 mm and a diameter of 30 mm. The cavitator is a disk with a thickness of 5 mm and a diameter of 15 mm, and it is connected to the underwater body through a cylinder-shaped rod that has a length of 10 mm and a diameter of 5 mm. The specific parameters of the model are given in Table 1. During the experiment, the air is ejected from a ventilation hole in the connecting rod that links the cavitator to the underwater body.

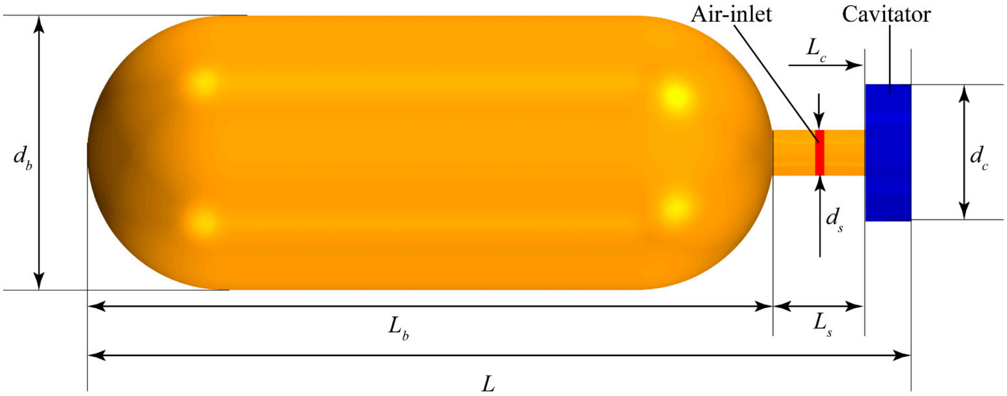

Figure 1. Geometric model and dimensional parameters.

Table 1. Main dimensional parameters of the model.

Name	Symbol	Size	Unit
Total length	L	90	mm
Main body length	L_b	75	mm
Main body diameter	d_b	30	mm
Cavitator length	L_c	5	mm
Cavitator diameter	d_c	15	mm
Connecting rod length	L_s	10	mm
Connecting rod diameter	d_s	5	mm

Figure 2 displays the computational domain and boundary conditions. The free surface was kept stationary in the calculation, and the immersion depth was altered by adjusting the position of the model. The model is located within a rectangular parallelepiped with dimensions of 7 L in height, 5 L in width, and 13 L in length. Here, L represents the total length of the model, which is L = 90 mm. The blockage ratio $(B = d_b/(5L) = 0.03/0.45 = 0.066\%)$ is far less than this value (5%), so the size of the computational domain will not affect the results [13]. At the inlet boundary, a uniform inflow condition is exerted with an inflow velocity of U = 4 m/s (based on experimental settings). The pressure outlet is set to a linear pressure proportional to the immersion depth, where the reference pressure is the free surface pressure, P_{atm} = 101,325 Pa. All other boundaries and the model's surface are defined as no-slip walls. To prevent reflected free surface waves, a wave damping region with a length of L is imposed close to the outlet boundary and sidewalls, as illustrated in Figure 3.

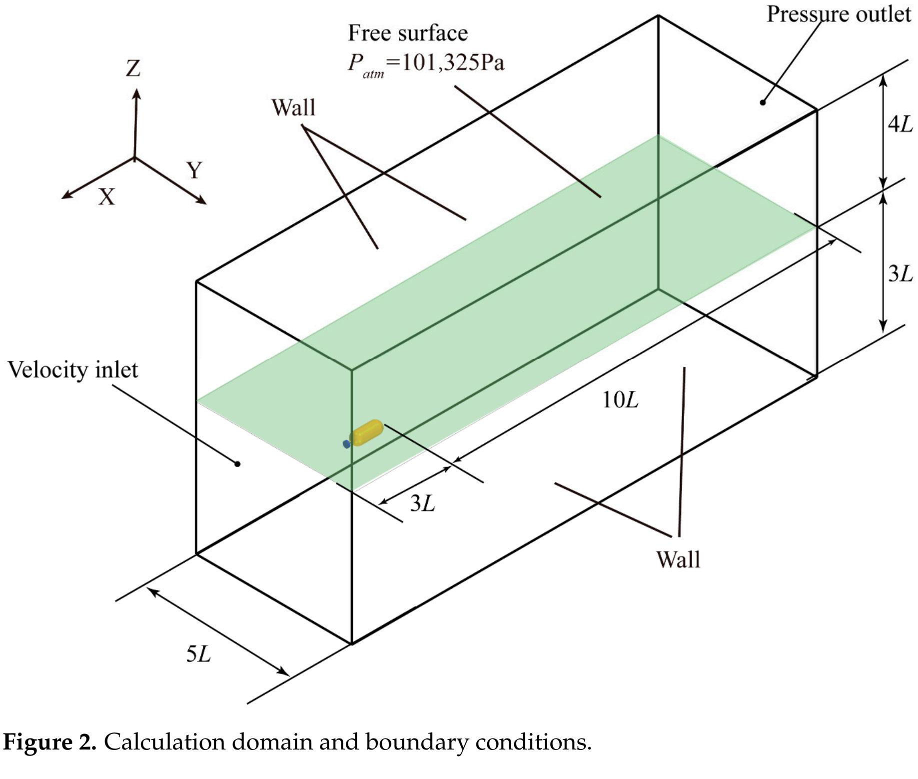

Figure 2. Calculation domain and boundary conditions.

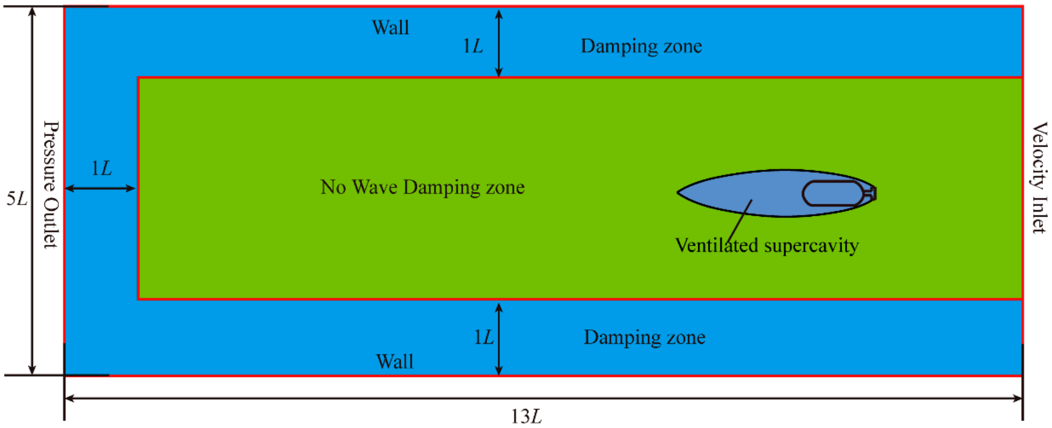

Figure 3. Schematic diagram of wave damping.

To better define the initial flow conditions for calculations, the main flow parameters were established and made dimensionless based on the cavitator diameter. The Froude number (F_{rd_c}), ventilation coefficient (C_{qd_c}), cavitation number (σ_c), and immersion depth ratio (h^*) are defined as follows:

$$F_{rd_c} = U/\sqrt{gd_c} F_{rd_c} = U/\sqrt{gd_c} \tag{10}$$

$$C_{qd_c} = Q/d_c^2 U C_{qd_c} = Q/d_c^2 U \tag{11}$$

$$\sigma_c = (p_{atm} + \rho g h_s - p_c)/(0.5\rho U^2) \tag{12}$$

$$h^* = h_s/d_c \tag{13}$$

Here, U represents the inlet boundary incoming flow velocity, g represents the acceleration of gravity, d_c represents the cavitator diameter, P_{atm} represents the standard atmospheric pressure, P_c represents the internal pressure of the ventilated supercavity, Q represents the volume flow rate, h_s represents the immersion depth, and ρ represents the density of water.

Figure 4 displays a schematic of the ventilated supercavity flow pattern close to the free surface, where U represents the free flow velocity, h_s represents the immersion depth of the model, L_{cav} represents the ventilated cavity length, O represents the origin point (0, 0, 0), and d_{cav} represents the ventilated cavity diameter.

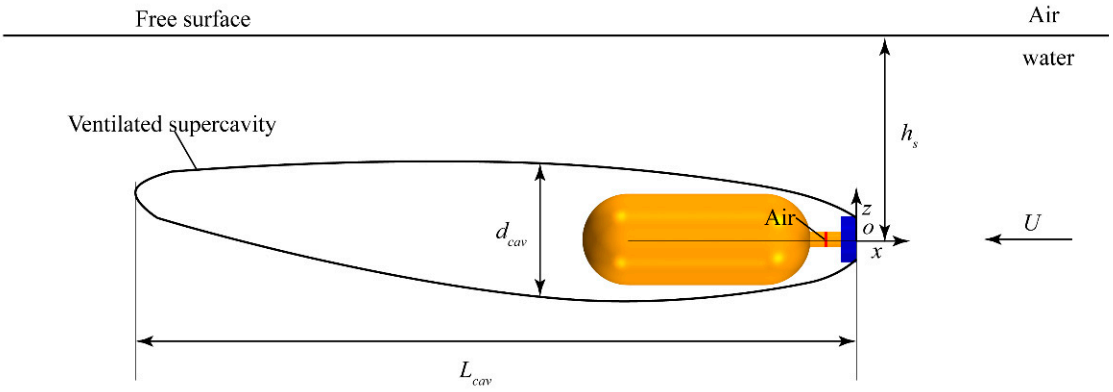

Figure 4. The schematic of the ventilated supercavity flow pattern close to the free surface.

To assess the influence of the free surface on the flow patterns of ventilated supercavities, the free surface was kept stationary in the calculation, and the immersion depth was altered by adjusting the position of the model. The immersion depths include h^* = 16.7, 5.7, 3.0, 2.0, 1.5, and 1.2, while the ventilation coefficient, Froude number, and cavitation number are maintained at constant values. Note that h^* = 16.7 represents an approximate infinite water depth, as per the literature. Consequently, under this immersion depth, the influence of the free surface on the ventilated supercavity is almost negligible. Conversely, h^* = 1.2 signifies that the model is nearly level with the free surface.

To solve the control equations in this study, the SIMPLE algorithm was utilized. The spatial term was discretized using a second-order upwind scheme, while the temporal term was discretized using a second-order implicit scheme. The convection term was discretized using the central difference method, and the high-resolution interface capturing (HRIC) scheme was applied to the volume of fluid (VOF) solution owing to its ability to track sharp interfaces between two immiscible phases. To capture the transient characteristic of cavitating flows, the time step was set as $\Delta t = T_{ref}/400 = 1.125 \times 10^{-4}$ s, where $T_{ref} = L/U$, which corresponds to the CFL $= 0.9$ and thus satisfies the calculation requirements [25]. The maximum internal iteration steps for unsteady simulations in each time step are 20 and the total numerical flow time in all cases is more than 1 s.

3.2. Mesh Details and Verification

The grid details are presented in Figure 5. To obtain high-resolution calculations for the ventilated supercavity and free surface, the Cartesian grid method with grid refinement was employed. A prism layer mesh and trimmed grid were subsequently established based on the surface grid to construct the volume grid. Regarding the near-wall grid, the boundary layer has 5 layers at a growth rate of 1.2, and thus the total thickness is 0.001 m. As recommended by Lv et al., the value of y + at the wall surface of the body is smaller than 60 [25]. Furthermore, the grid size around the model in the radial direction was approximately 1×10^{-3} m. Additionally, a finer grid was adopted close to the free surface with a sizing of 5×10^{-4} m. This complies with the suggested grid resolution for free surfaces set by ITTC [45].

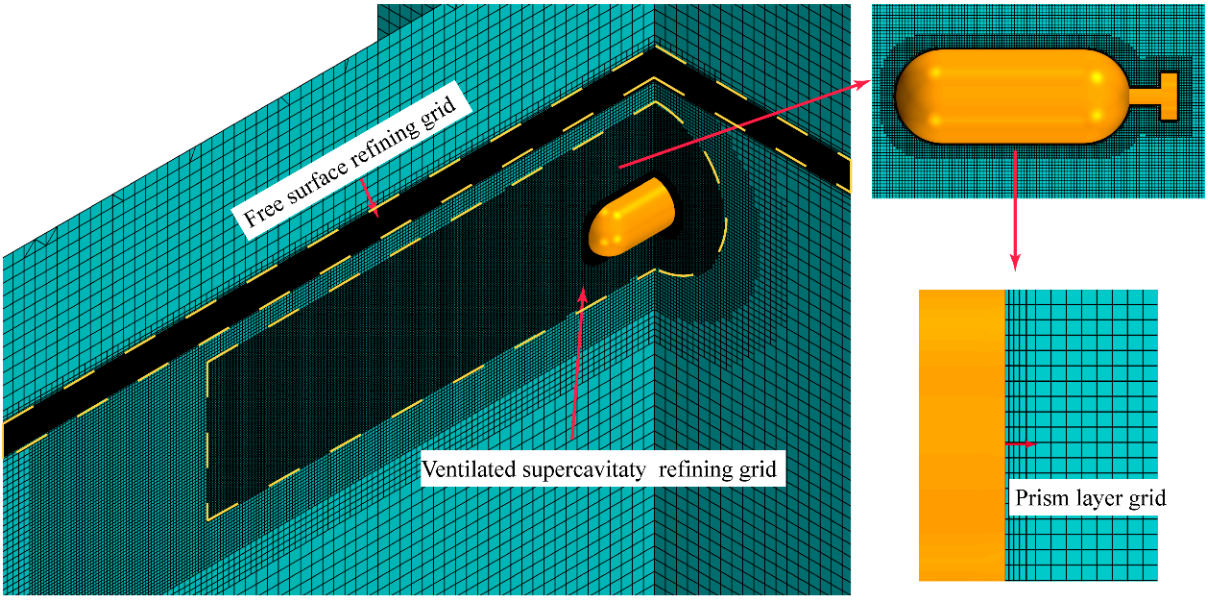

Figure 5. Grid details.

To verify the grid independence of the ventilated supercavity close to the free surface, three sets of grids were utilized. The grid details used in this study are described in Section 3.2, with the refinement ratio set to be $\tau = N_2/N_1 = N_3/N_2 = 2$, where N_1, N_2, and N_3 represent the grid numbers of the coarse, medium, and fine mesh, respectively. The coarse mesh has about 2.81 million grid nodes, the medium mesh has approximately 5.74 million grid nodes, and the fine mesh has around 11.9 million grid nodes.

Figure 6 displays the ventilated supercavity obtained from experiments and numerical simulations based on three sets of grids under fully submerged conditions (F_{rd_c} = 10.4, C_{qd_c} = 0.25, c = 0.08, h^* = 16.7). In addition, Figure 7 shows the ventilated supercavity under shallowly submerged conditions (F_{rd_c} = 10.4, C_{qd_c} = 0.25, c = 0.08, h^* = 5.7). In Figures 6 and 7, the blue isosurface (α_v = 0.1) represents the ventilated supercavity obtained from numerical simulations, while the cyan isosurface (α_g = 0.5) represents the free surface, the experimental data reprinted with permission from Ref. [12]. 2018, Jaeho Chung and Yeunwoo Cho. It can be observed that both the cavity geometry obtained from the calculations are in agreement with the experimental findings, and the gas leakage mode at the closure region is also consistent with the experiments, with a twin-vortex tube gas leakage mode being identified [12]. The shapes of the ventilated supercavity obtained from different grids are generally similar, with some differences in closure region position. This discrepancy is primarily due to a finer grid that more accurately captures the gas–liquid interface.

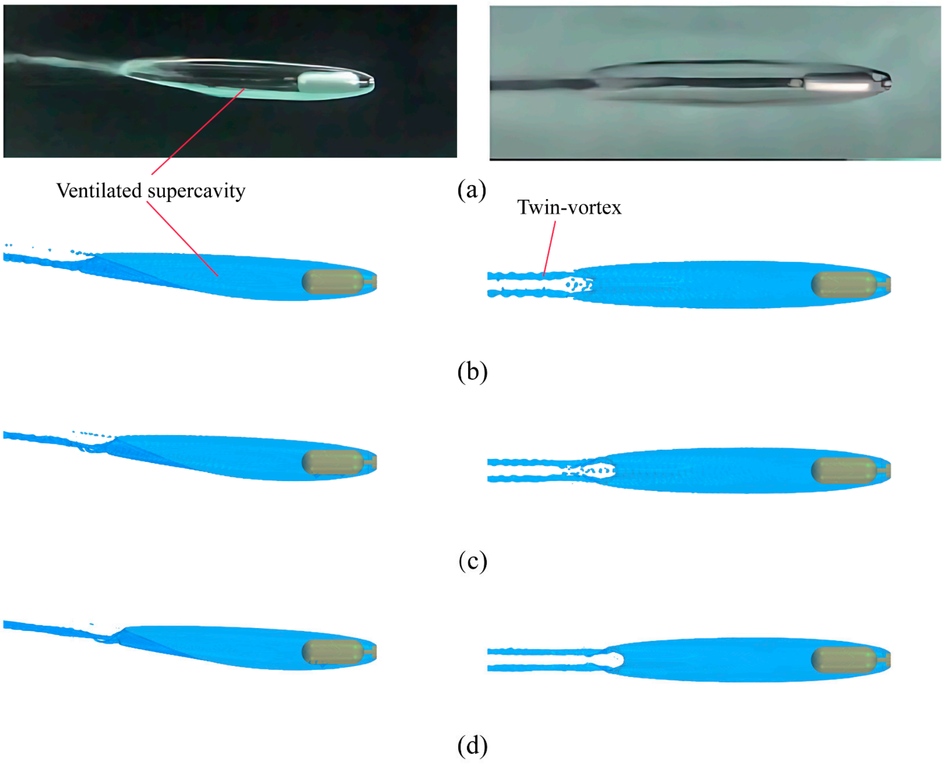

(a)

(b)

(c)

(d)

Figure 6. Comparison of the ventilated supercavity under fully submerged conditions (F_{rd_c} = 10.4, C_{qd_c} = 0.25, c = 0.08, h^* = 16.7), where the ventilated supercavity obtained from numerical simulations is shown using blue isosurface (α_v = 0.1). (**a**) Experiment, (**b**) coarse, (**c**) medium, (**d**) fine grid.

Figure 8 compares the ventilated supercavity obtained from the experiments and numerical simulations. Figure 8a displays the fully submerged condition (F_{rd_c} = 10.4, C_{qd_c} = 0.25, c = 0.08, h^* = 16.7), while Figure 8b illustrates the shallowly submerged condition (F_{rd_c} = 10.4, C_{qd_c} = 0.25, c = 0.08, h^* = 5.7). The geometric dimensions of the ventilated cavity obtained from the three sets of grids have small errors when compared to the experimental results. However, there is a relatively large error at the cavity closure region due to the strong unsteadiness and gas leakage occurring at this position. As the geometric shapes of the free surface and cavity obtained from the three sets of grids are almost identical, a medium mesh is selected as the final mesh to balance computational cost and accuracy.

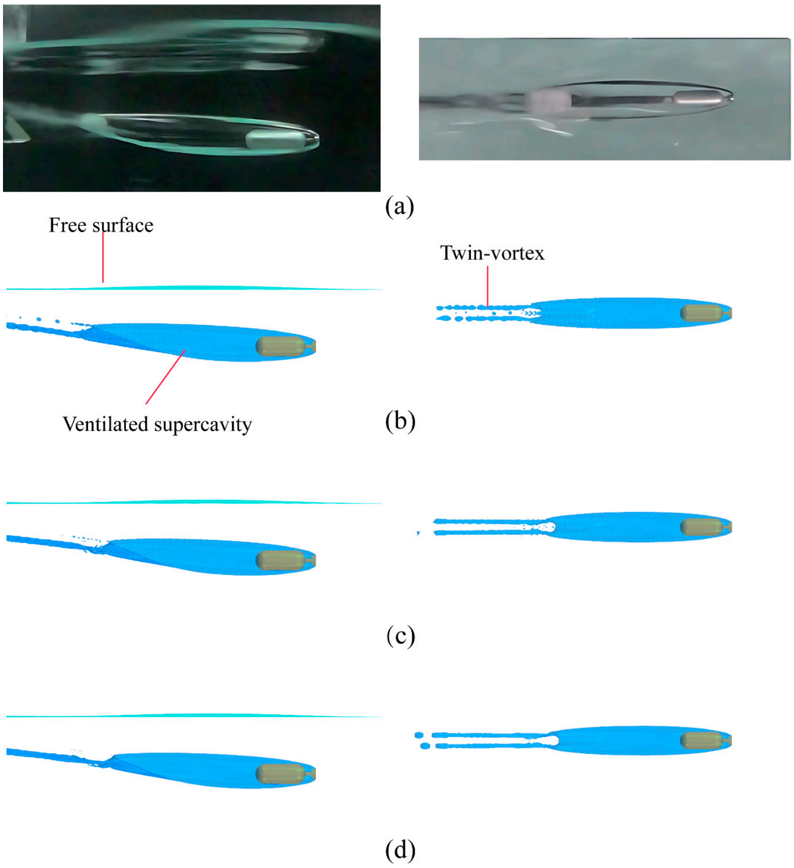

Figure 7. Comparison of the ventilated supercavity under shallowly submerged conditions (F_{rd_c} = 10.4, C_{qd_c} = 0.25, c = 0.08, h^* = 5.7), where the ventilated supercavity obtained from numerical simulations is shown using blue isosurface (α_v = 0.1) and the free surface is shown using cyan isosurface (α_g = 0.5). (**a**) Experiment, (**b**) coarse, (**c**) medium, (**d**) fine grid.

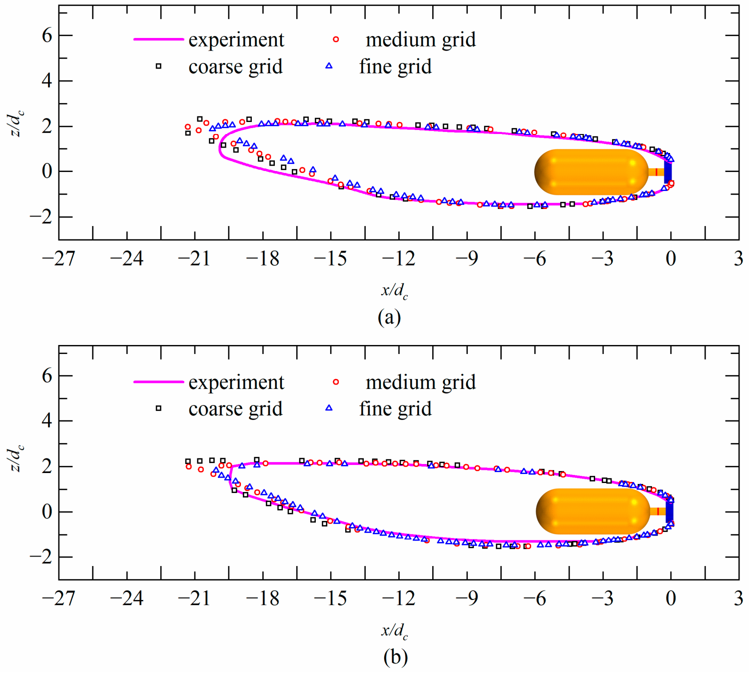

Figure 8. Comparison of the ventilated supercavity obtained from the experiments and numerical simulations. (**a**) Fully submerged condition (F_{rd_c} = 10.4, C_{qd_c} = 0.25, c = 0.08, h^* = 16.7); (**b**) shallowly submerged condition (F_{rd_c} = 10.4, C_{qd_c} = 0.25, c = 0.08, h^* = 5.7).

4. Results and Discussion

4.1. Effect of Free Surface on the Supercavity Shape

Figure 9 show the free surface shapes and ventilated supercavity shapes at different immersion depth conditions (h^* = 16.7, 5.7, 3.0, 2.0, 1.5, and 1.2), where the blue isosurface (α_v = 0.1) represents the ventilated supercavity obtained from numerical simulations, while the cyan isosurface (α_g = 0.5) represents the free surface. Additionally, Figure 10 show the shape of the ventilated supercavity at the mid-longitudinal plane for various immersion depth conditions. It is observed that when the immersion depth is large, the ventilated supercavity is significantly influenced by gravity and exhibits obvious asymmetry, with the ventilated supercavity shifted upwards relative to the model's symmetry line. A reduction in immersion depth results in a more pronounced effect of the free surface on the ventilated supercavity. This weakens the gravity influence and causes the tail of the supercavity to shift downwards when compared to conditions at greater immersion depths. Additionally, the gas leakage mode at the ventilated supercavity closure region has changed. Under high immersion conditions (h^* = 16.7, h^* = 5.7, and h^* = 3.0), the air inside the ventilated supercavity leaks through two hollow tubes at the tail, exhibiting a typical twin-vortex tube, as shown in Figure 9a–c. Under low-immersion conditions (h^* = 2.0, h^* = 1.5, and h^* = 1.2), the twin-vortex tube was shed under the action of the re-entrant jet, as shown in Figure 9d–f.

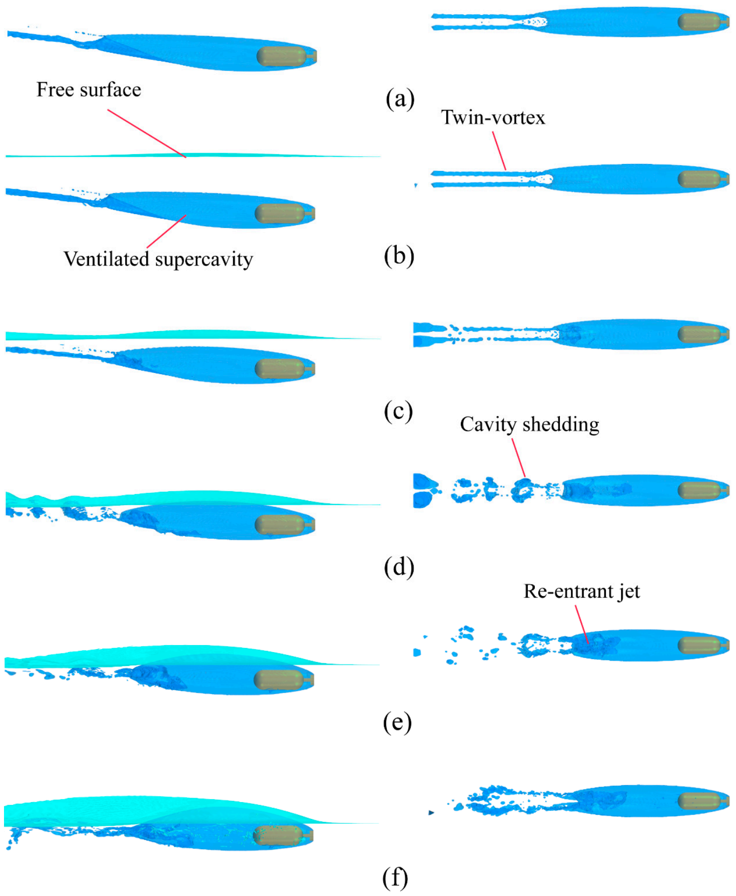

Figure 9. Free surface and ventilated supercavity for various immersion depths, where the blue isosurface (α_v = 0.1) depicts the ventilated supercavity obtained from numerical simulations, while the cyan isosurface (α_g = 0.5) represents the free surface. Left: main view; right: top view. (**a**) h^* = 16.7, (**b**) h^* = 5.7, (**c**) h^* = 3.0, (**d**) h^* = 2.0, (**e**) h^* = 1.5, (**f**) h^* = 1.2.

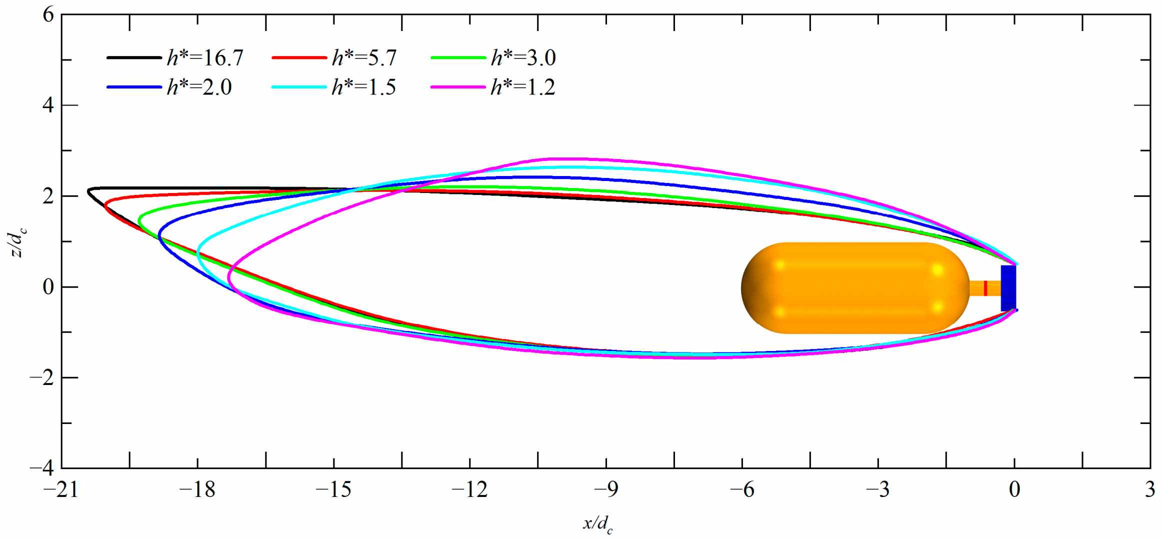

Figure 10. The shape of the ventilated supercavity at the mid-longitudinal plane for various immersion depth conditions (h^* = 16.7, 5.7, 3.0, 2.0, 1.5, and 1.2).

Figure 11 presents the relationship between the cavity length and immersion depth, with the vertical axis representing the dimensionless length of the ventilated supercavity based on the cavitator diameter and the horizontal axis representing the dimensionless immersion depth based on the cavitator diameter. Meanwhile, Figure 12 shows the relationship between the maximum diameter of the ventilated supercavity and immersion depth, with the vertical axis representing the dimensionless maximum diameter based on the cavitator diameter and the horizontal axis representing the dimensionless immersion depth based on the cavitator diameter. It is observed that as the immersion depth decreases, the ventilated supercavity length decreases, and the maximum diameter increases. The primary reason for this trend is that the distance between the free surface and the upper surface of the ventilated supercavity decreases, the vertical velocity between the two becomes shorter and the pressure difference between the two leads to higher acceleration of the fluid pointing towards the ventilated supercavity, which increases the cavity curvature and shortens the cavity length [34]. The specific mechanism of the interaction between the free surface and the ventilated supercavity is explained in Section 4.4.

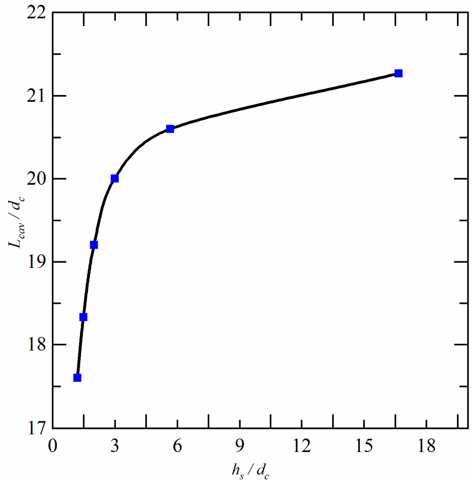

Figure 11. Relationship between length of the ventilated supercavity and immersion depth.

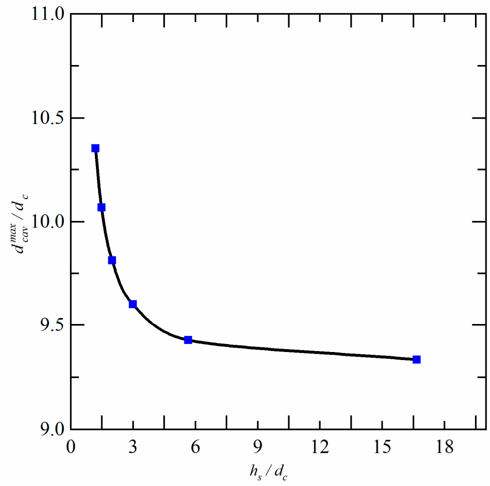

Figure 12. Relationship between the ventilated supercavity maximum diameter and immersion depth.

Figure 13 presents the ventilated supercavity shape at different cross sections for various immersion depth conditions (h^* = 16.7, 5.7, 3.0, 2.0, 1.5, and 1.2). At high immersion depths, the ventilated supercavity curves upward along the center line of the model, and the ventilated supercavity's cross section is deformed at the tail, forming a "crescent" region with a high void fraction. Additionally, two hollow tubes are formed in the far flow field of the ventilated supercavity through which air is leaked, as shown in Figure 13a,b. Ventilated cavity buoyancy is related to the gravity effect. At shallow immersion depths, the flow pattern inside the ventilated supercavity is more complex, with gas and water chaotically distributed. Additionally, the gas–water distribution in the circumferential direction exhibits high asymmetry, primarily attributed to the impact of the re-entrant jet [25], as shown in Figure 13c,d.

4.2. Flow Structure and Gas Leakage Behavior under the Influence of Free Surface

Figure 14 depicts the velocity distribution of the ventilated supercavity with different immersion depth conditions, with the left side showing the middle longitudinal section and the right side showing the cross section at various locations. The internal flow field of the ventilated cavity is classified into three regions: the internal boundary layer, the ventilation influence region, and the reverse flow region. The ventilation influence region is primarily located at the back of the cavitator, where ventilation jets are ejected from the ventilation holes. The boundary layer region is located near the ventilated supercavity surface and is parallel to the mainstream. The reverse flow region is located at the ventilated supercavity center and is opposite in direction to the mainstream. Under high-immersion conditions (h^* = 16.7, h^* = 5.7, and h^* = 3.0), the reverse flow region at the ventilated supercavity tail presents a typical crescent shape and forms two hollow tubes with the same direction as the mainstream moving downstream. This indicates that the ventilated supercavity mainly drains downstream through two hollow tubes, as shown in Figure 14a–c. On the other hand, for shallow immersion conditions (h^* = 2.0, h^* = 1.5, and h^* = 1.2), the flow characteristics in the wake of the ventilated supercavity are more intricate, consisting of forward and reverse-flow patterns within the reverse flow region, predominantly influenced by the presence of the free surface. The shape of the reverse flow region is irregular as a result of the re-entrant jet, as presented in Figure 14d–f.

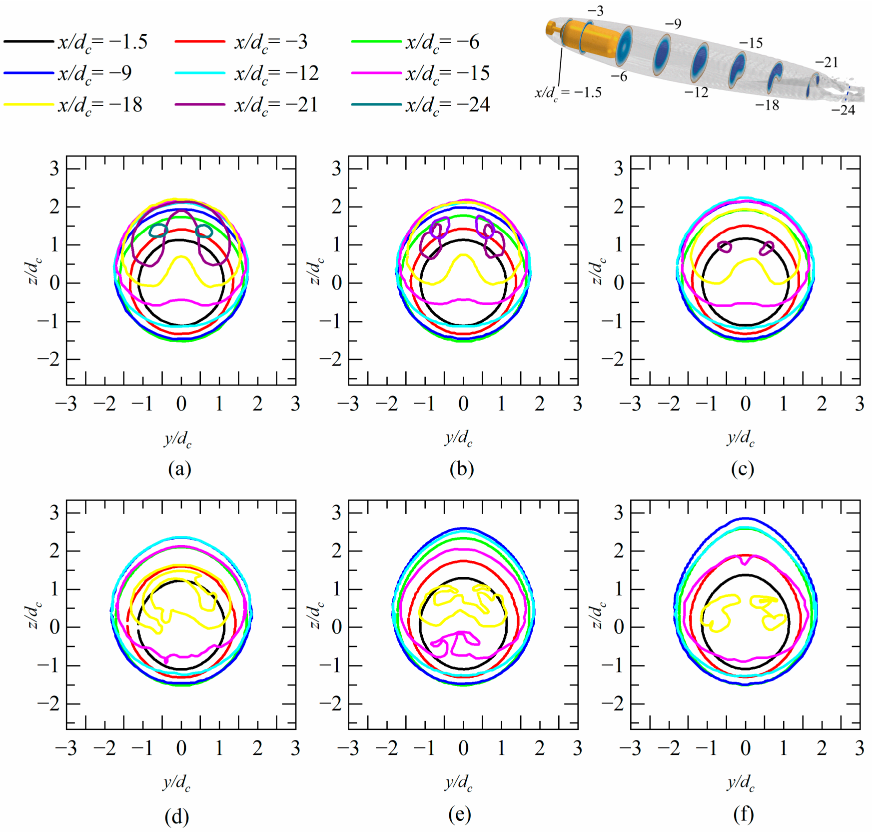

Figure 13. The ventilated supercavity shape at different cross sections for various immersion depth conditions. (**a**) h^* = 16.7, (**b**) h^* = 5.7, (**c**) h^* = 3.0, (**d**) h^* = 2.0, (**e**) h^* = 1.5, (**f**) h^* = 1.2.

Figure 15 illustrates the velocity profiles for various positions (i.e., x/d_c = −3, −6, −9, −12, −15, −18, −21, and −24), where the vertical axis is the dimensionless vertical position based on the cavitator diameter and the horizontal axis is the dimensionless axial velocity based on the inlet incoming velocity. Negative values on the horizontal axis represent the same direction as the mainstream, while positive values indicate the opposite direction. Figure 15 displays the presence of internal boundary layers on both the upper and lower portions of the model. However, due to the 3D asymmetry of the cavity, only a thin region of the reverse flow is visible at the model's upper surface. As it moves downstream, the internal boundary layer thickness changes, due to a larger reverse flow region formed at the ventilated cavity center. The direction of the internal gas flow gradually aligns with the mainstream under the influence of water flow viscosity, resulting in a visible zero-velocity strip between the internal boundary layer and the reverse flow region.

To gain a deeper understanding of the gas leakage mechanism, velocity vectors were drawn and are presented in Figure 16. The velocity disparity leads to the creation of two counterrotating trailing vortices at the ventilated supercavity tail, and both rotating trailing vortices form an upward velocity at the ventilated supercavity centerline, creating the two hollow tubes under the continuous action of two counterrotating trailing vortices [29], as shown in Figure 16a,b. The free surface influences the development of the re-entrant jet at the ventilated supercavity closure region. The twin-vortex tube ruptures into a bubbly flow that sheds and moves downward under the influence of the re-entrant jet, as shown in Figure 16d,e.

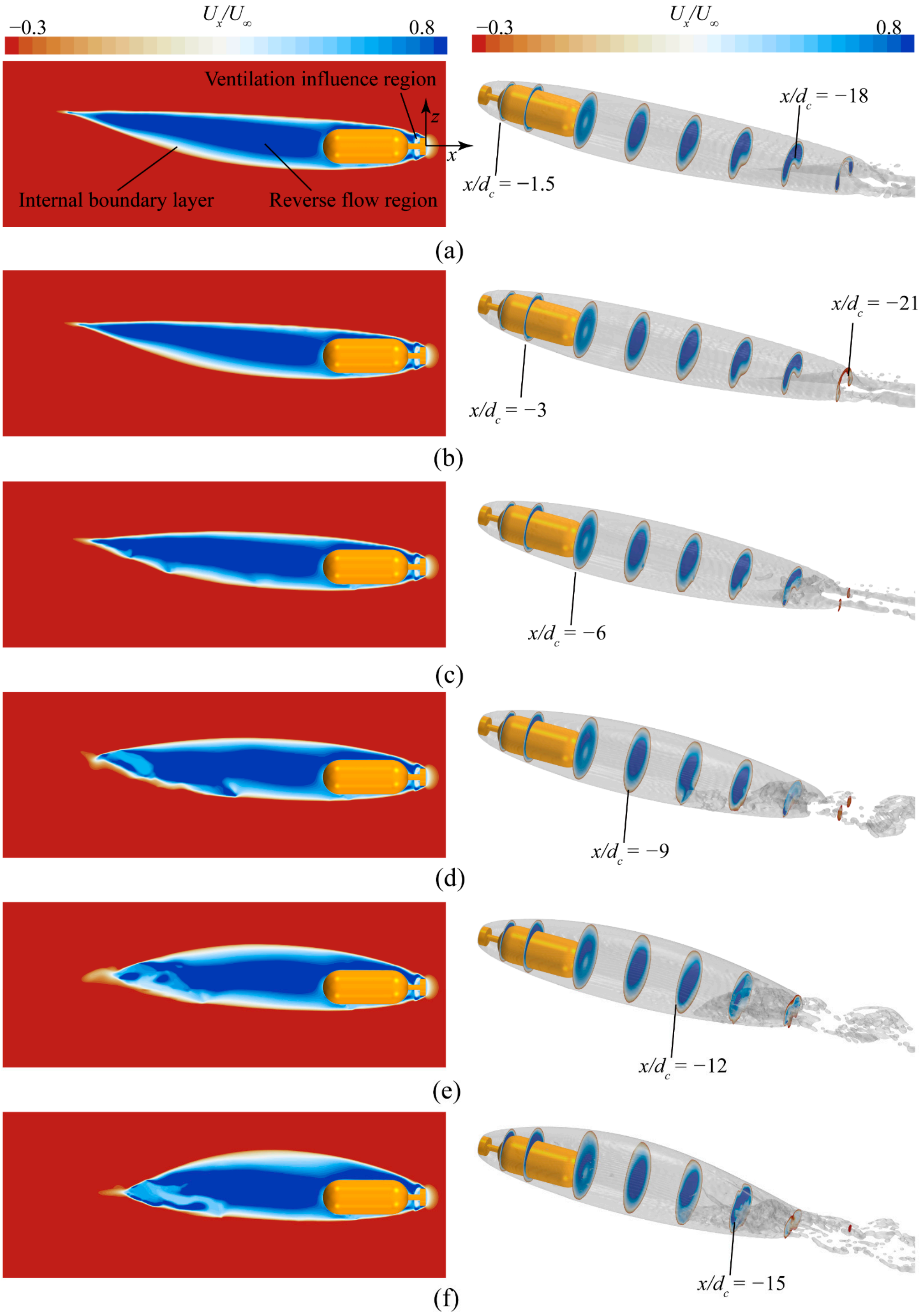

Figure 14. The velocity distribution of the ventilated supercavity under different immersion depth conditions, with the left side showing the middle longitudinal section and the right side showing the cross section at various locations. (**a**) $h^* = 16.7$, (**b**) $h^* = 5.7$, (**c**) $h^* = 3.0$, (**d**) $h^* = 2.0$, (**e**) $h^* = 1.5$, (**f**) $h^* = 1.2$.

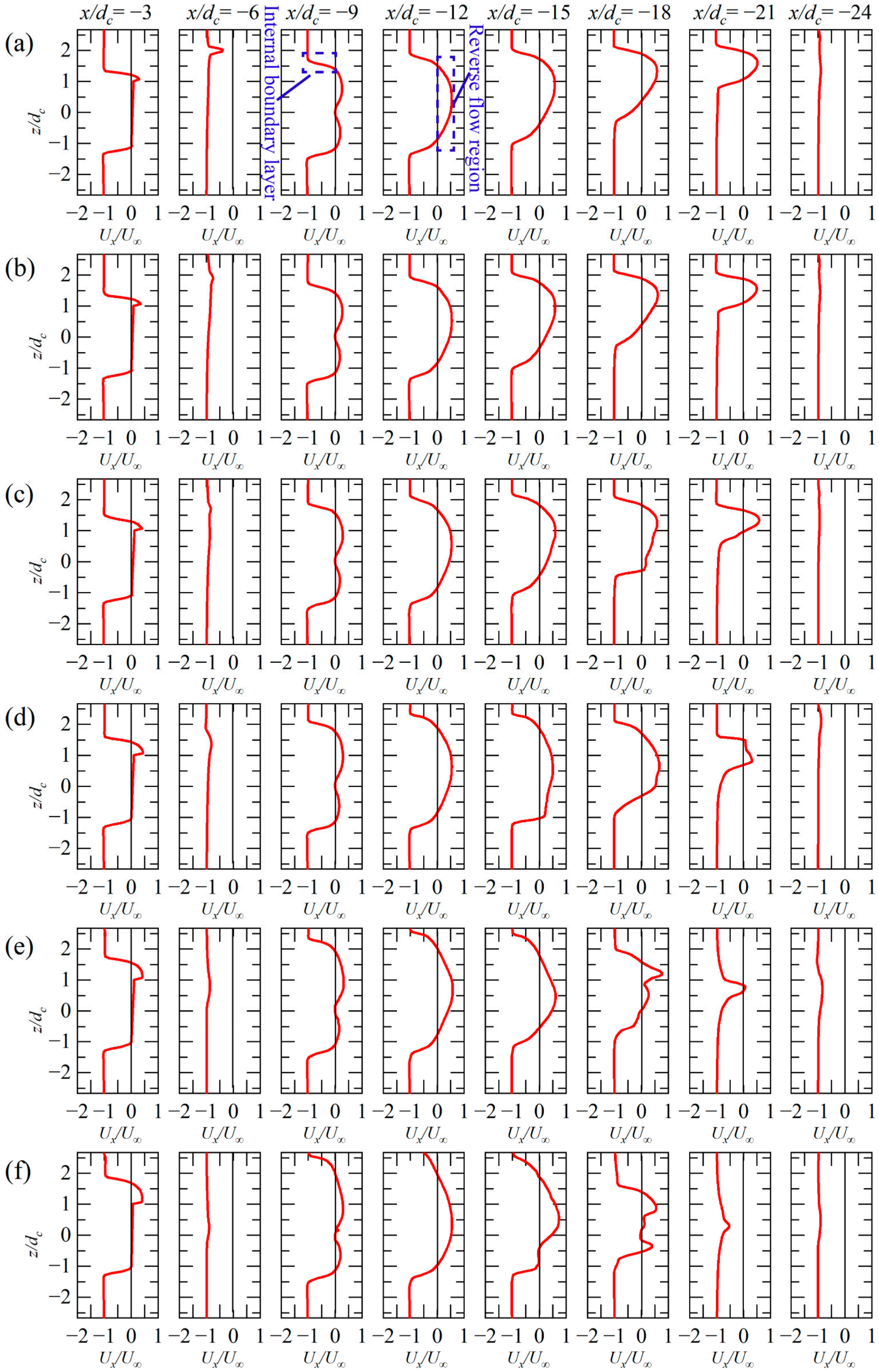

Figure 15. The velocity profiles for various positions (i.e., $x/d_c = -3, -6, -9, -12, -15, -18, -21$, and -24). (**a**) $h^* = 16.7$, (**b**) $h^* = 5.7$, (**c**) $h^* = 3.0$, (**d**) $h^* = 2.0$, (**e**) $h^* = 1.5$, (**f**) $h^* = 1.2$.

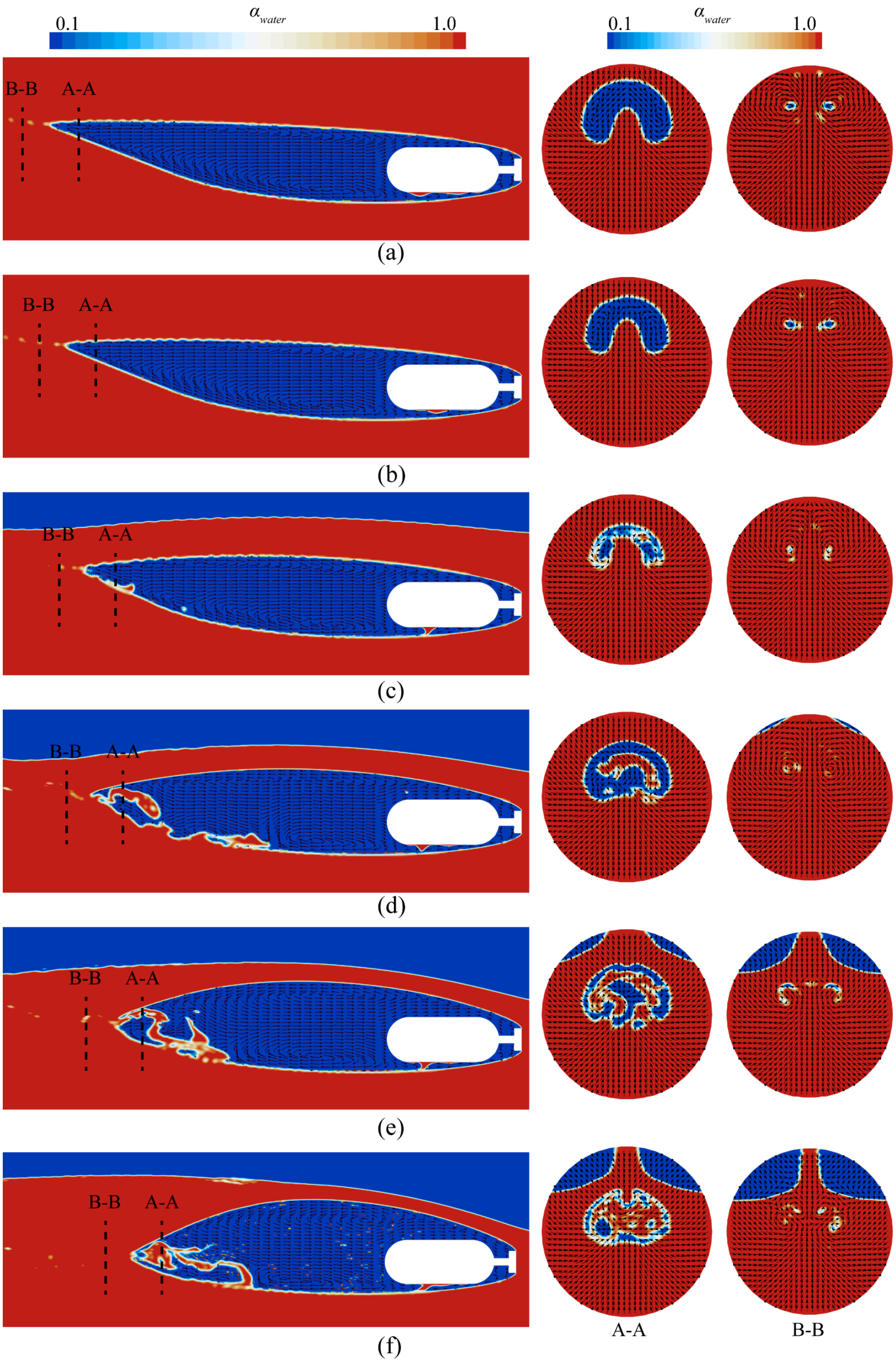

Figure 16. Velocity vectors inside the cavity and near the cavity tail. (**a**) $h^* = 16.7$, (**b**) $h^* = 5.7$, (**c**) $h^* = 3.0$, (**d**) $h^* = 2.0$, (**e**) $h^* = 1.5$, (**f**) $h^* = 1.2$.

To gain further insight into the generation of the re-entrant jet, an analysis of the pressure gradient in the ventilated supercavity was conducted. The position of the monitoring line and the distribution of the pressure gradient on the monitoring line are displayed in Figures 17 and 18, respectively. The monitoring line is situated in the mid-longitudinal plane immediately above the model's upper surface, as depicted in Figure 17. A significant peak in the pressure gradient was observed at the ventilated supercavity closure region, indicating the presence of a strong adverse pressure gradient in the gas–water interface near the ventilated supercavity closure [25,46]. The adverse pressure gradient resulting from low pressure inside the ventilated supercavity and high pressure at the ventilated supercavity closure causes flow separation, causing water penetration into the interior of the cavity through the air–water interface as a re-entrant jet. As the immersion depth decreases, the pressure gradient peak at the cavity closure region becomes more pronounced, leading to a greater likelihood of the re-entrant jet breaking through the air–water interface. Ultimately, the twin-vortex tube at the cavity closure ruptures into a bubbly flow and periodically sheds under the continuous influence of the re-entrant jet.

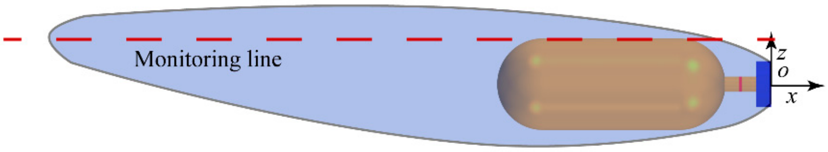

Figure 17. Schematic diagram of the monitoring line.

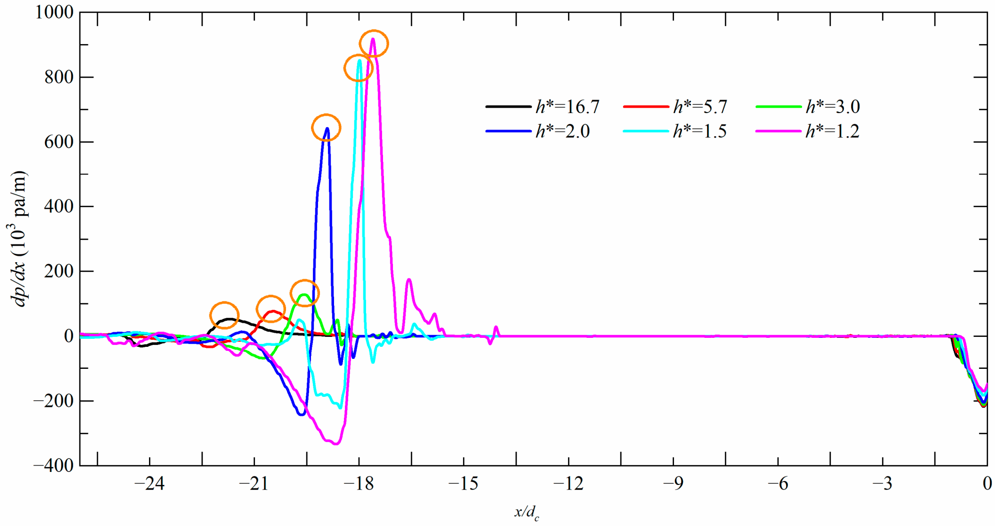

Figure 18. Variation in pressure gradient in the flow direction for different immersion depths.

Figure 19 presents the flow structure and gas leakage mode under the effect of the free surface. Specifically, Figure 19a depicts a schematic diagram of the high-immersion condition, and Figure 19b displays the schematic diagram of the shallow-immersion condition. The ventilation influence region is primarily located at the back of the cavitator, where ventilation jets are ejected from the ventilation holes. There is a reverse region and an internal boundary layer downstream of the ventilated cavity. For the internal boundary layer region, the gas velocity increases from zero to the same velocity as the water flow in the same direction. For the reverse flow region, two zero-velocity bands can be observed near the model. One zero velocity band separates the internal boundary layer and the reverse flow region, while the other zero-velocity band is present at the model's surface. A more significant reverse region exists behind the tail of the model. At high immersion depths, two hollow tubes form at the cavity end, and air leaks through these tubes, resulting in a typical twin-vortex tube leakage mode. On the other hand, for shallow immersion depths, the twin-vortex tube at the cavity closure ruptures into a bubbly flow and periodically sheds under the continuous influence of the re-entrant jet.

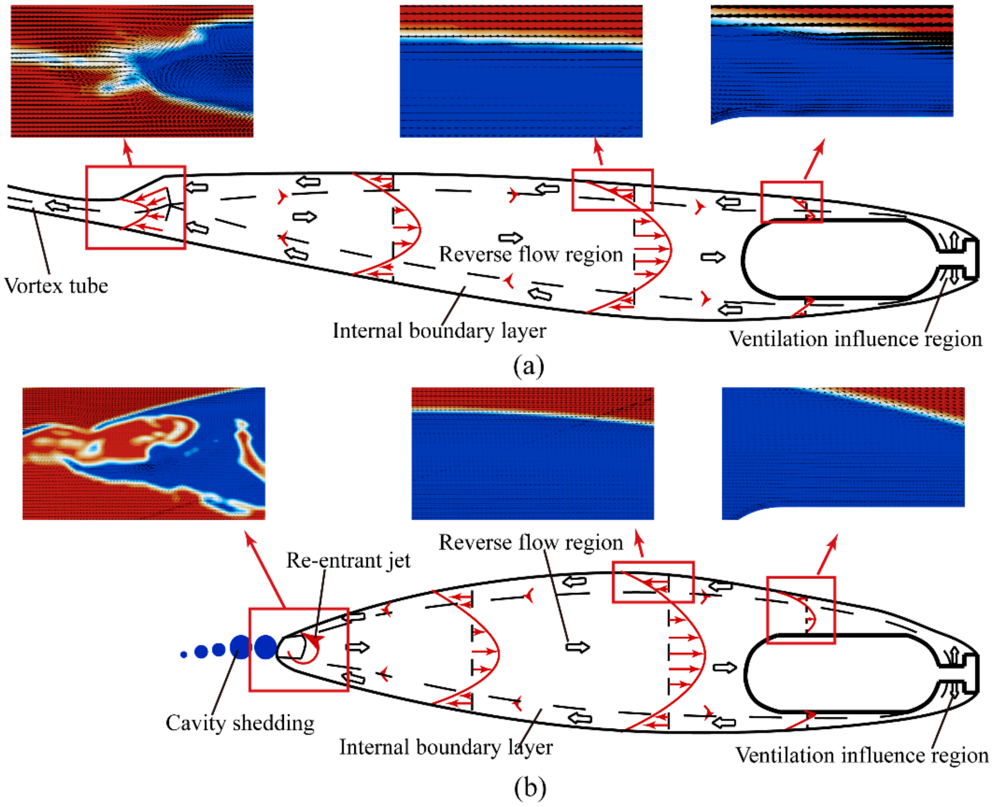

Figure 19. Schematic diagram of the flow structure and gas leakage modes inside the ventilated supercavity. (**a**) High immersion depth; (**b**) shallow immersion depth.

4.3. Deformation of Free Surface

Figures 20 and 21 present the free surface at different immersion depths, respectively. The free surface deformation is a dimensionless height based on the cavitator diameter, where the free surface dimensionless height is defined as $z^* = (z - z_0)/d_c$, with z_0 being the free surface original vertical coordinate, z being the free surface vertical coordinate after perturbation, and d_c being the cavitator diameter. As the immersion depth decreases, the deformation of the free surface increases, mainly because the free surface is more influenced by the model at shallow immersion depth. Near the ventilated supercavity, the shape of the free surface is similar to that of the ventilated supercavity. At a position far from the ventilated supercavity, the shape of the free surface depends on the type of ventilated supercavity leakage.

In the twin-vortex tube leakage mode, the ventilated supercavity is steadily leaked through the twin-vortex tubes. The twin-vortex tube floats up under the gravity effect, which causes the deformation of the free surface, illustrated in Figure 21. In the re-entrant jet leakage mode, the twin-vortex tube has periodic cavity shedding, causing the free surface to deform periodically. As the immersion depth decreases, the free surface is deformed to the same shape as the geometry of the ventilated cavity.

4.4. The Influence Mechanism between the Free Surface and the Ventilated Supercavity

To further investigate the influence mechanism between the free surface and the ventilated supercavity, velocity vectors and vertical velocity distributions are plotted in Figures 22 and 23. Figure 23 represents the dimensionless vertical velocity based on the incoming flow velocity, where the red indicates positive vertical velocity with the direction pointing to the free surface and the blue indicates negative vertical velocity with the direction pointing to the ventilated supercavity upper surface. Without the effect of the free surface, the vertical velocity is mainly positive near the ventilated supercavity upper surface, and the negative vertical velocity at the cavity tail is almost negligible. As the distance between the free surface and the ventilated supercavity becomes shorter, the positive vertical velocity increases at the head of the cavity, while the negative vertical velocity increases at the trailing part of the cavity. The cavity curvature increases and decreases in length under the continuous action of the front and rear vertical velocity.

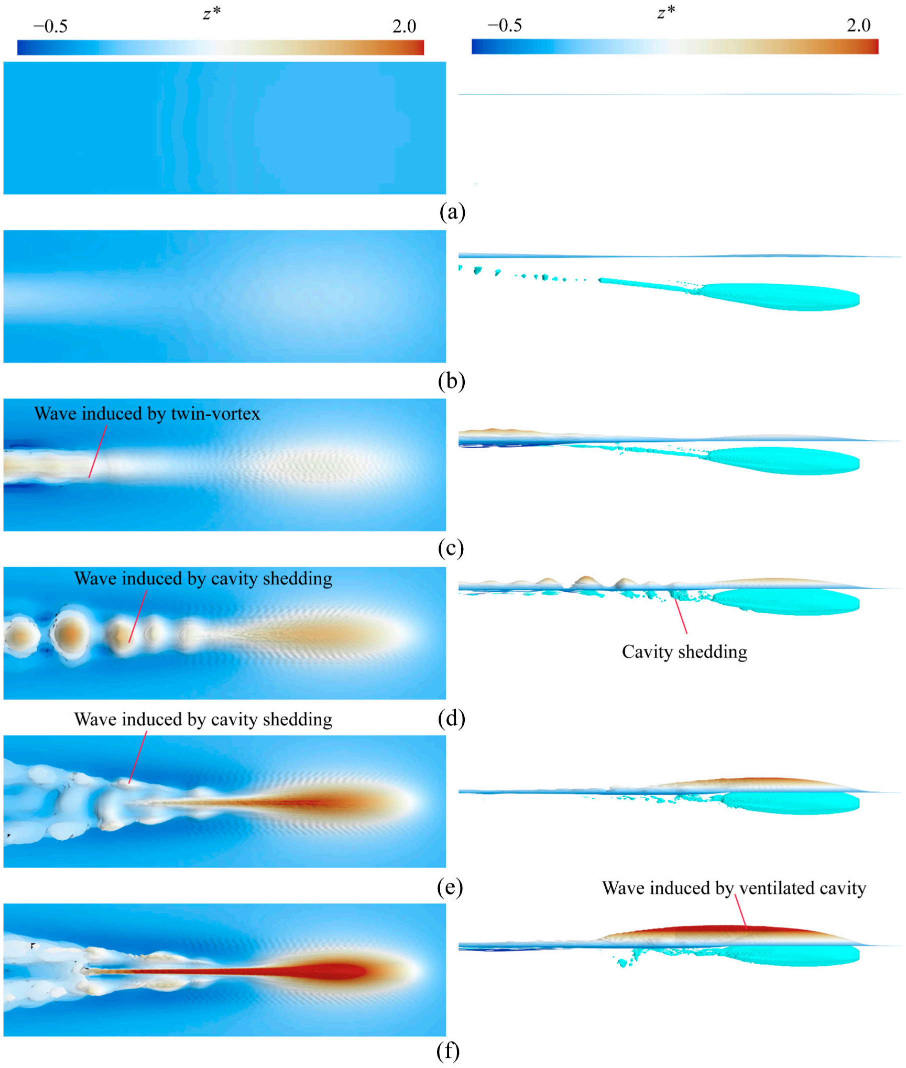

Figure 20. Shapes of the free surface at different immersion depths. (**a**) $h^* = 16.7$, (**b**) $h^* = 5.7$, (**c**) $h^* = 3.0$, (**d**) $h^* = 2.0$, (**e**) $h^* = 1.5$, (**f**) $h^* = 1.2$.

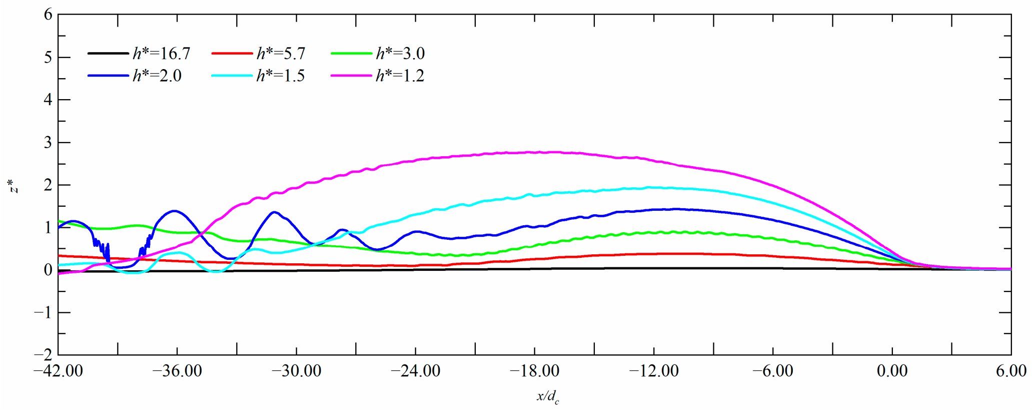

Figure 21. Free surface deformation.

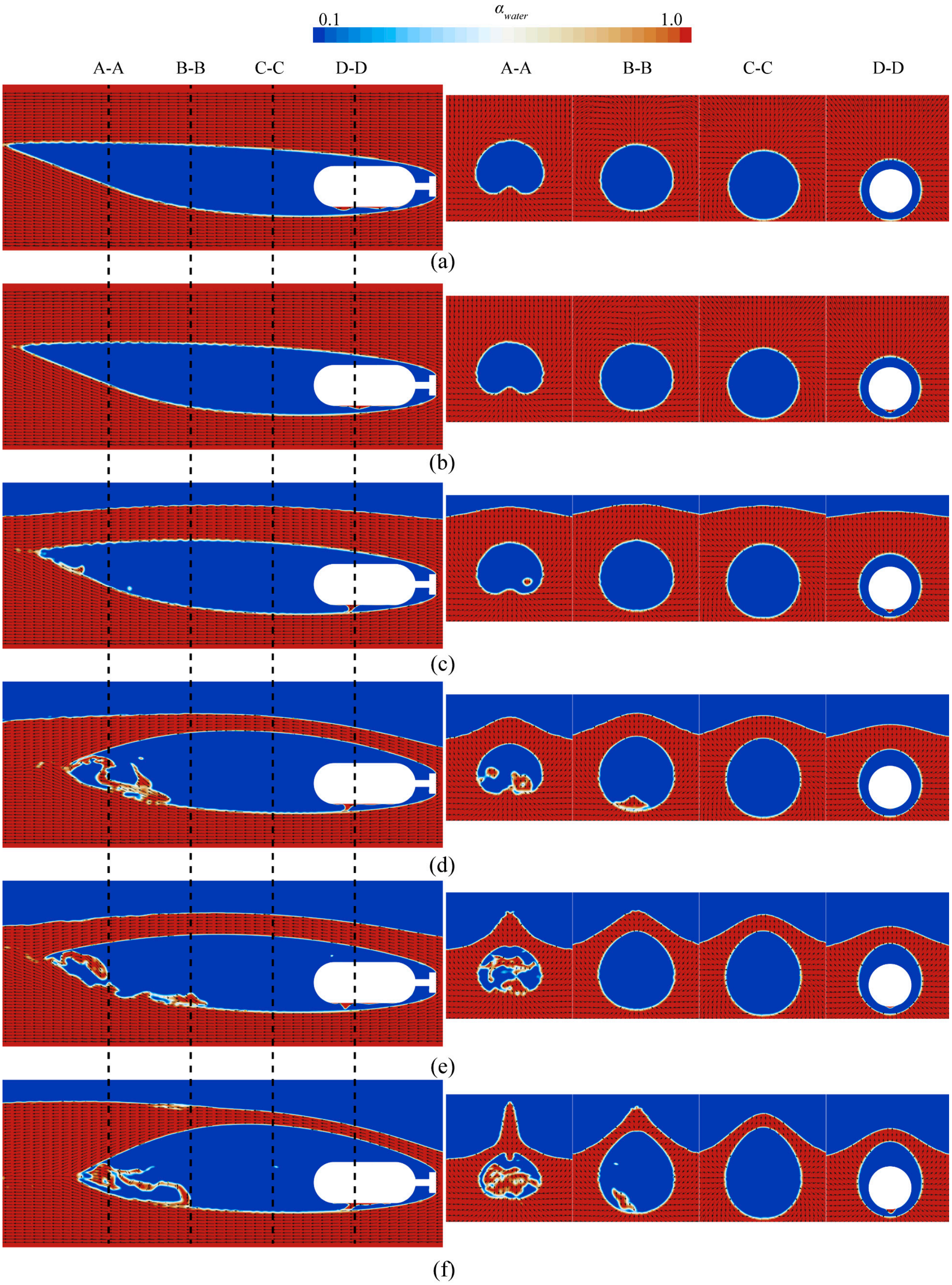

Figure 22. Velocity vectors near the ventilated supercavity. (**a**) $h^* = 16.7$, (**b**) $h^* = 5.7$, (**c**) $h^* = 3.0$, (**d**) $h^* = 2.0$, (**e**) $h^* = 1.5$, (**f**) $h^* = 1.2$.

Figure 24 is a schematic diagram of the influence mechanism between the free surface and the ventilated supercavity. When the effect of the free surface is negligible, the vertical momentum of the ventilated supercavity cannot overcome the buoyancy force, causing the phenomenon of upward floating, with the vertical velocity on the upper surface of the cavity pointing upwards, and the ventilated supercavity is mainly affected by the gravity effect. When the ventilated cavity is near the free surface, the ventilated supercavity is affected by both the free surface effect and the gravity effect. The upward floating of the ventilated supercavity induced by gravity causes the deformation of the free surface, which assumes a shape consistent with that of the ventilated supercavity. The flow between the upper surface of the ventilated cavity and the free surface is directed towards the latter at the leading part and towards the former at the trailing part, due to the influence of free surface effects. The curvature of the ventilated supercavity increases and its length decreases under the persistent impact of the flow.

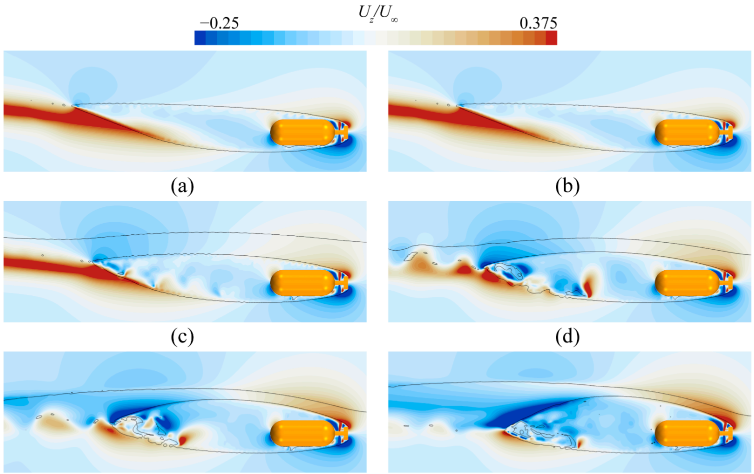

(a) (b)

(c) (d)

(e) (f)

Figure 23. Vertical velocity distribution between the free surface and the ventilated supercavity upper surface. (**a**) $h^* = 16.7$, (**b**) $h^* = 5.7$, (**c**) $h^* = 3.0$, (**d**) $h^* = 2.0$, (**e**) $h^* = 1.5$, (**f**) $h^* = 1.2$.

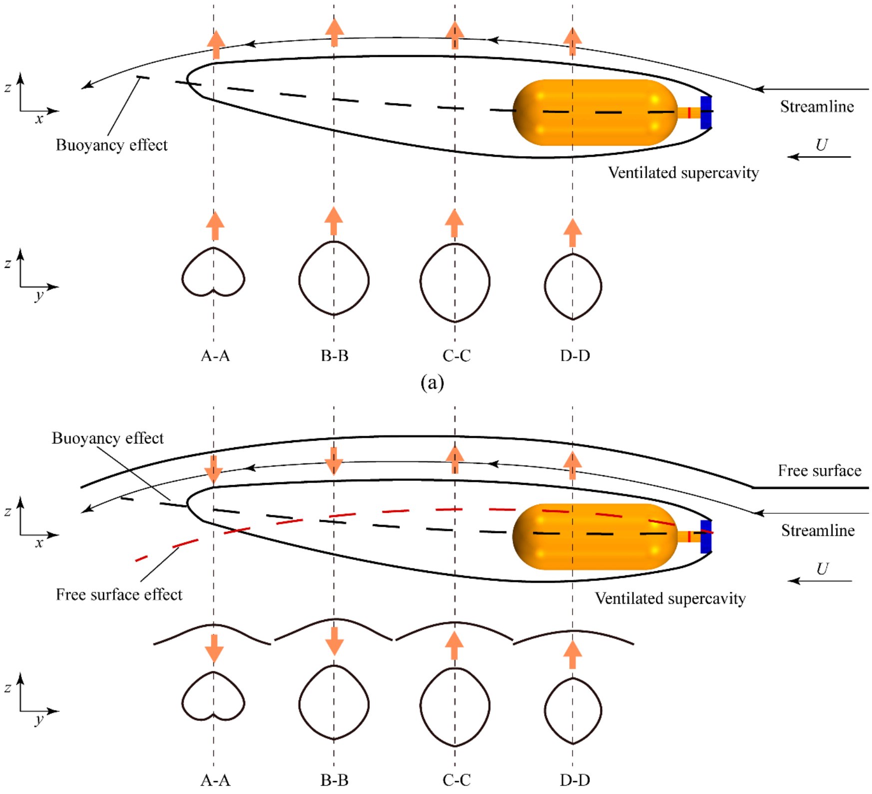

(a)

(b)

Figure 24. Schematic diagram of the influence mechanism between the free surface and the ventilated supercavity. (**a**) Without free surface; (**b**) with the free surface.

5. Conclusions

The ventilated supercavity near the free surface was investigated by numerical simulation in this paper. The cavity geometry, the internal flow structure, the closure mode, and the interaction mechanism with the free surface were analyzed. The conclusions are drawn as follows.

(1) The length and diameter of the ventilated supercavity predicted by numerical simulation are consistent with the experimental data. Ventilated cavities are asymmetrical under the influence of gravity. As the immersion depth decreases, the ventilated supercavity length decreases, and the maximum diameter increases.

(2) Twin-vortex tube leakage mode is observed at high immersion depths, and re-entrant jet leakage mode is observed at shallow immersion depths. For the twin-vortex tube leakage mode, the cavity is symmetrical from left to right, while for the re-entrant jet leakage mode, the cavity has asymmetry at the tail.

(3) The internal flow field of the ventilated supercavity is classified into three regions: the internal boundary layer, the ventilation influence region, and the reverse flow region. For shallow immersion conditions ($h^* = 2.0$, $h^* = 1.5$, and $h^* = 1.2$), the flow characteristics in the wake of the ventilated supercavity are more intricate, mainly due to the free surface, a stronger reverse pressure gradient is formed at the cavity closure, which promotes flow separation.

(4) The interaction mechanism between the free surface and the ventilated cavity is through the vertical velocity between the two. When the ventilated supercavity is affected by both the free surface effect and the gravity effect, the gravity effect causes the ventilated supercavity to float upward, and the free surface effect alters the flow near the upper surface of the ventilated supercavity, leading to an increase in the curvature and a decrease in the length of the ventilated supercavity.

Author Contributions: Conceptualization, Y.Z. and J.Z.; methodology, Y.Z. and J.Z.; software, Y.Z.; formal analysis, Y.Z. and R.H.; investigation, Y.Z. and J.Z.; resources, J.Z., R.H. and Y.W.; data curation, Y.Z. and R.H.; writing—original draft preparation, Y.Z.; writing—review and editing, J.Z., R.H. and Y.W.; supervision, Y.W. and N.L.; project administration, J.Z., N.L. and Y.W.; funding acquisition, J.Z., N.L. and Y.W. All authors have read and agreed to the published version of the manuscript.

Funding: This work is supported by Shenzhen Science and Technology Program (JCYJ20220818102012024). The authors would like to gratefully acknowledge the National Natural Science Foundation of China (52006232).

Institutional Review Board Statement: Not applicable.

Informed Consent Statement: Not applicable.

Data Availability Statement: Not applicable.

Conflicts of Interest: The authors declare no conflict of interest.

References

1. Xiang, M.; Li, K.; Tu, J.; Zhang, H. Numerical investigation on the gas entrainment of ventilated partial cavity based on a multiscale modelling approach. *Appl. Ocean Res.* **2016**, *60*, 84–93. [CrossRef]
2. Jiang, Y.; Jeong, S.-W.; Ahn, B.-K.; Kim, H.-T.; Jung, Y.-R. Experimental investigation of drag characteristics of ventilated supercavitating vehicles with different body shapes. *Phys. Fluids* **2019**, *31*, 052106. [CrossRef]
3. Zhou, H.; Xiang, M.; Zhang, W.; Xu, X.; Zhao, K.; Zhao, S. Interaction between Natural and ventilated cavitation around a Base ventilated hydrofoil. *J. Appl. Fluid Mech.* **2019**, *12*, 1873–1883. [CrossRef]
4. Ceccio, S.L. Friction drag reduction of external flows with bubble and gas injection. *Annu. Rev. Fluid Mech.* **2010**, *42*, 183–203. [CrossRef]
5. Wang, Z.; Huang, B.; Zhang, M.; Wang, G. Experimental and numerical investigation of ventilated cavitating flow structures with special emphasis on vortex shedding dynamics. *Int. J. Multiph. Flow* **2018**, *98*, 79–95. [CrossRef]
6. Harwood, C.M.; Young, Y.L.; Ceccio, S.L. Ventilated cavities on a surface-piercing hydrofoil at moderate Froude numbers: Cavity formation, elimination and stability. *J. Fluid Mech.* **2016**, *800*, 5–56. [CrossRef]
7. Yoon, K.; Li, J.; Shao, S.; Karn, A.; Hong, J. Investigation of ventilation demand variation in unsteady supercavitation. *Exp. Therm. Fluid Sci.* **2021**, *129*, 110472. [CrossRef]

8. Huang, R.; Qiu, R.; Zhi, Y.; Wang, Y. Investigations into the ventilated cavities around a surface-piercing hydrofoil at high Froude numbers. *Phys. Fluids* **2022**, *34*, 043304. [CrossRef]
9. Shiri, A.; Leer-Andersen, M.; Bensow, R.E.; Norrby, J. Hydrodynamics of a displacement air cavity ship. In Proceedings of the 29th Symposium on Naval Hydrodynamics, Gothenburg, Sweden, 26–31 August 2012.
10. Mäkiharju, S.A.; Ganesh, H.; Ceccio, S.L. The dynamics of partial cavity formation, shedding and the influence of dissolved and injected non-condensable gas. *J. Fluid Mech.* **2017**, *829*, 420–458. [CrossRef]
11. Wu, Y.; Liu, Y.; Shao, S.; Hong, J. On the internal flow of a ventilated supercavity. *J. Fluid Mech.* **2019**, *862*, 1135–1165. [CrossRef]
12. Chung, J.; Cho, Y. Ventilated supercavitation around a moving body in a still fluid: Observation and drag measurement. *J. Fluid Mech.* **2018**, *854*, 367–419. [CrossRef]
13. Karn, A.; Arndt, R.E.; Hong, J. An experimental investigation into supercavity closure mechanisms. *J. Fluid Mech.* **2016**, *789*, 259–284. [CrossRef]
14. Shao, S.; Karn, A.; Ahn, B.-K.; Arndt, R.E.; Hong, J. A comparative study of natural and ventilated supercavitation across two closed-wall water tunnel facilities. *Exp. Therm. Fluid Sci.* **2017**, *88*, 519–529. [CrossRef]
15. Karn, A.; Ellis, C.; Arndt, R.; Hong, J. An integrative image measurement technique for dense bubbly flows with a wide size distribution. *Chem. Eng. Sci.* **2015**, *122*, 240–249. [CrossRef]
16. Cao, L.; Karn, A.; Arndt, R.E.; Wang, Z.; Hong, J. Numerical investigations of pressure distribution inside a ventilated supercavity. *J. Fluids Eng.* **2017**, *139*, 021301. [CrossRef]
17. Qin, S.; Wu, Y.; Wu, D.; Hong, J. Experimental investigation of ventilated partial cavitation. *Int. J. Multiph. Flow* **2019**, *113*, 153–164. [CrossRef]
18. Barbaca, L.; Pearce, B.W.; Brandner, P.A. Experimental study of ventilated cavity flow over a 3-D wall-mounted fence. *Int. J. Multiph. Flow* **2017**, *97*, 10–22. [CrossRef]
19. Qin, S.; Sun, S.; Yoon, K.; Fang, H.; Chen, Y.; Wu, D. Investigation on the internal flow of ventilated partial cavity. *Phys. Fluids* **2021**, *33*, 083303. [CrossRef]
20. Zhou, H.; Xiang, M.; Zhao, S.; Zhang, W. Development of a multiphase cavitation solver and its application for ventilated cavitating flows with natural cavitation. *Int. J. Multiph. Flow* **2019**, *115*, 62–74. [CrossRef]
21. Rashidi, I.; Pasandideh-Fard, M.; Passandideh-Fard, M.; Nouri, N. Numerical and experimental study of a ventilated supercavitating vehicle. *J. Fluids Eng.* **2014**, *136*, 101301. [CrossRef]
22. Qin, S.; Sun, S.; Fang, H.; Wang, L.; Chen, Y.; Wu, D. Experimental and numerical investigation on the cavity regime and drag reduction of ventilated partial cavity. *Ocean Eng.* **2021**, *234*, 109257. [CrossRef]
23. Mousavi, S.M.; Roohi, E. On the effects of hybrid surface wettability on the structure of cavitating flow using implicit large eddy simulation. *J. Taiwan Inst. Chem. Eng.* **2023**, 104828. [CrossRef]
24. Pendar, M.-R.; Alavi, A.; Roohi, E. Identification of frequency modes and spectral content for noise suppression: Cavitationow over 3-D hydrofoil with sinusoidal leading edge. *Int. J. Mod. Phys. C* **2023**, *2350074*, 19. [CrossRef]
25. Lv, Y.; Zhang, M.; Liu, T.; Chen, J.; Huang, B.; Hao, L. Physical and numerical study on the transition of gas leakage regime of ventilated cavitating flow. *Ocean Eng.* **2021**, *239*, 109861. [CrossRef]
26. Bin, J.; Luo, X.-w.; Peng, X.-x.; Zhang, Y.; Wu, Y.-l.; Xu, H.-y. Numerical investigation of the ventilated cavitating flow around an under-water vehicle based on a three-component cavitation model. *J. Hydrodyn. Ser. B* **2010**, *22*, 753–759.
27. Jiang, C.-X.; Shuai, Z.-J.; Zhang, X.-Y.; Li, W.-Y.; Li, F.-C. Numerical study on evolution of axisymmetric natural supercavitation influenced by turbulent drag-reducing additives. *Appl. Therm. Eng.* **2016**, *107*, 797–803. [CrossRef]
28. Zhang, X.; Wang, C.; Wekesa, D.W. Numerical and experimental study of pressure-wave formation around an underwater ventilated vehicle. *Eur. J. Mech.-B/Fluids* **2017**, *65*, 440–449. [CrossRef]
29. Wang, Z.; Huang, B.; Wang, G.; Zhang, M.; Wang, F. Experimental and numerical investigation of ventilated cavitating flow with special emphasis on gas leakage behavior and re-entrant jet dynamics. *Ocean Eng.* **2015**, *108*, 191–201. [CrossRef]
30. Xu, C.; Huang, J.; Wang, Y.; Wu, X.; Huang, C.; Wu, X. Supercavitating flow around high-speed underwater projectile near free surface induced by air entrainment. *AIP Adv.* **2018**, *8*, 035016. [CrossRef]
31. Wang, Y.; Xu, C.; Wu, X.; Huang, C.; Wu, X. Ventilated cloud cavitating flow around a blunt body close to the free surface. *Phys. Rev. Fluids* **2017**, *2*, 084303. [CrossRef]
32. Faltinsen, O.M.; Semenov, Y.A. The effect of gravity and cavitation on a hydrofoil near the free surface. *J. Fluid Mech.* **2008**, *597*, 371–394. [CrossRef]
33. Xu, C.; Khoo, B.C. Numerical investigation on the cloud cavitating flow over a Clark Y foil under free surface effect. *Ocean Eng.* **2022**, *266*, 112953. [CrossRef]
34. Liu, B.; Xiang, M.; Xie, Z.; Zhang, W. On ventilated supercavities moving horizontally near free surface. *Ocean Eng.* **2023**, *267*, 113229. [CrossRef]
35. Moltani, A.-A.; PasandidehFard, M.; Erfanian, M.-R. Experimental and numerical study of free surface effect on the ventilated cavitating flow around a surface vehicle model. *Ocean Eng.* **2023**, *268*, 113413. [CrossRef]
36. Xu, C.; Wang, Y.; Huang, C.; Yu, C.; Huang, J. Cloud cavitating flow that surrounds a vertical hydrofoil near the free surface. *J. Fluids Eng.* **2017**, *139*, 101302. [CrossRef]
37. Xu, C.; Huang, J.; Yu, C.; Wang, Y.; Huang, C.; Khoo, B.C. Free surface and near-wall effects on the cloud cavitating flow over an axisymmetric projectile. *Ocean Eng.* **2021**, *238*, 109682. [CrossRef]

38. Xu, C.; Wang, Y.; Huang, C.; Yu, C.; Huang, J. Analysis of Near-wall effect on cloud cavitating flow that surrounds an axisymmetric projectile using large eddy simulation with Cartesian cut-cell mesh method. *Eur. J. Mech.-B/Fluids* **2018**, *67*, 15–24. [CrossRef]
39. Xu, C.; Wang, Y.; Huang, C.; Huang, J.; Yu, C. The effect of free surface on cloud cavitating flow around a blunt body. *J. Hydrodyn. Ser. B* **2017**, *29*, 979–986. [CrossRef]
40. Zhi, Y.; Huang, R.; Qiu, R.; Wang, Y.; Huang, C. LES investigation into the cavity shedding dynamics and cavitation–vortex interaction around a surface-piercing hydrofoil. *Phys. Fluids* **2022**, *34*, 123314. [CrossRef]
41. An, H.; Pan, H.; Yang, P. CFD-based numerical study on drag reduction of ventilated supercavities combined with gas layer of the surface vehicle with struts. *Ocean Eng.* **2022**, *262*, 112334. [CrossRef]
42. Zhi, Y.; Zhang, Z.; Huang, R.; Qiu, R.; Wang, Y. Numerical investigations into supercavitating flows and hydrodynamic characteristics of a heaving hydrofoil. *Mod. Phys. Lett. B* **2022**, *36*, 2150605. [CrossRef]
43. Spalart, P.R.; Rumsey, C.L. Effective inflow conditions for turbulence models in aerodynamic calculations. *AIAA J.* **2007**, *45*, 2544–2553. [CrossRef]
44. Choi, J.; Yoon, S.B. Numerical simulations using momentum source wave-maker applied to RANS equation model. *Coast. Eng.* **2009**, *56*, 1043–1060. [CrossRef]
45. Spence, S. *Numerical Investigation of Free Surface Flows*; Institutt for Marin Teknikk: Trondheim, Norway, 2014.
46. Yang, Q.; Wang, C.; Wei, Y.; Wang, Y.; Zhang, D.; Hu, X. Experimental study on the collapse of tail cavity induced by underwater ventilation. *Phys. Fluids* **2022**, *34*, 112111. [CrossRef]